icy satellites (*4*) had severely strained the shadow-hiding models (*6*, *7*) but are easily explained by coherent backscatter. This phenomenon also accounts for the enhanced brightnesses of lunar rays near full moon, which shadow-hiding models have difficulty explaining.

These results also have implications for terrestrial remote sensing from aircraft and Earth orbiters. Like soil, vegetation exhibits an opposition effect, which is known to agronomists as the hot spot. Because of the large sizes and separations of leaves in vegetation compared with the wavelength, it is likely that most of the hot spot is caused by shadow hiding. However, individual leaves also exhibit an opposition peak (*5*), which may be caused by coherent backscatter between cells and other microscopic elements of the leaves. Which effect dominates the hot spot in vegetation remains to be determined.

Because shadow hiding must also occur in planetary regoliths, it is unlikely that coherent backscatter is the only cause of opposition effects. However, it appears that coherent backscatter dominates most of the opposition peaks observed in the solar system.

REFERENCES AND NOTES

1. T. Gehrels, *Astrophys. J.* **123**, 331 (1956). In this paper, Gehrels introduced the term "opposition effect."
2. H. Seeliger, *Abh. Bayer. Akad. Wiss. Math. Naturwiss. Kl. Sitzungsber.* **16**, 405 (1887); **18**, 1 (1895). Seeliger analyzed observations by G. Muller [*Publ. Astrophys. Obs. Potsdam No. 30* **8**, 193 (1893)].
3. T. Gehrels *et al.*, *Astron. J.* **69**, 826 (1964); P. Oetking, *J. Geophys. Res.* **71**, 2505 (1966); E. Whitaker, in "Analysis of Apollo 8 Photography and Visual Observations," *NASA SP-201*, 38 (1969); W. Egan and T. Hilgeman, *Appl. Opt.* **15**, 1845 (1976); T. Thorpe, *Icarus* **36**, 204 (1978); R. L. Wildey, *Science* **200**, 1265 (1978); W. Montgomery and R. Kohl, *Opt. Lett.* **5**, 546 (1980); A. Harris *et al.*, *Icarus* **81**, 365 (1989).
4. R. Brown and D. Cruikshank, *Icarus* **55**, 83 (1983); D. Domingue *et al.*, *ibid.* **90**, 30 (1991); D. T. Thompson and G. W. Lockwood, *J. Geophys. Res.* **97**, 14761 (1992).
5. P. Woessner and B. Hapke, *Remote Sensing Environ.* **21**, 243 (1987).
6. B. Hapke, *J. Geophys. Res.* **68**, 4571 (1963); W. Irvine, *ibid.* **71**, 2931 (1966); K. Lumme and E. Bowell, *Astron. J.* **86**, 1694 (1981).
7. B. Hapke, *Icarus* **67**, 264 (1986).
8. K. Watson, *J. Math. Phys.* **10**, 688 (1969).
9. Y. Kuga and A. Ishimaru, *J. Opt. Soc. Am. A* **1**, 831 (1984).
10. P. Wolf and G. Maret, *Phys. Rev. Lett.* **55**, 2696 (1985); F. MacKintosh and S. John, *Phys. Rev. B* **37**, 1884 (1988); K. Peters, *ibid.* **46**, 801 (1992); for a recent review, see A. McGurn, *Surf. Sci. Rep.* **10**, 357 (1990).
11. B. Hapke, *Icarus* **88**, 407 (1990); _____ and D. Blewett, *Nature* **352**, 46 (1991).
12. Y. Shkuratov, *Kinematics Phys. Celestial Bodies* **4**, 33 (1988); M. Mishchenko and J. Dlugach, *Mon. Not. R. Astron. Soc.* **254**, 15 (1992).
13. K. Muinonen, thesis, University of Helsinki (1990).
14. Y. Shkuratov, *Sol. Syst. Res.* **23**, 111 (1989).
15. B. Lyot, *Ann. Obs. Paris* **VIII**, 1 (1929).
16. D. McKay *et al.*, in *Proceedings of the Fifth Lunar Science Conference*, W. A. Gose, Ed. (Pergamon, New York, 1974), pp. 887–906.
17. D. Harris, in *Planets and Satellites*, G. Kuiper and B. Middlehurst, Eds. (Univ. of Chicago Press, Chicago, 1961), pp. 272–342.
18. S. Ostro and E. Shoemaker, *Icarus* **85**, 335 (1990).
19. K. O'Donnell and E. Mendez, *J. Opt. Soc. Am. A* **4**, 1194 (1987).
20. M. Mishchenko, *Astrophys. Space Sci.* **194**, 327 (1992).
21. For clarity, data for only one state of incident polarization are shown; curves for orthogonal states are almost identical.

22. We acknowledge the contributions of V. Gharakanian, L. Horn, and P. Hererra to the measurements reported here. This research was supported by grants from the Planetary Geology and Geophysics Program, Office of Space Science and Applications, National Aeronautics and Space Administration.

2 November 1992; accepted 4 March 1993

Manganese Oxide Octahedral Molecular Sieves: Preparation, Characterization, and Applications

Y. F. Shen, R. P. Zerger, R. N. DeGuzman, S. L. Suib,* L. McCurdy, D. I. Potter, C. L. O'Young*

A thermally stable 3 × 3 octahedral molecular sieve corresponding to natural todorokite (OMS-1) has been synthesized by autoclaving layer-structure manganese oxides, which are prepared by reactions of MnO_4^- and Mn^{2+} under markedly alkaline conditions. The nature and thermal stability of products depend strongly on preparation parameters, such as the MnO_4^-/Mn^{2+} ratio, pH, aging, and autoclave conditions. The purest and the most thermally stable todorokite is obtained at a ratio of 0.30 to 0.40. Autoclave treatments at about 150° to 180°C for more than 2 days yield OMS-1, which is as thermally stable (500°C) as natural todorokite minerals. Adsorption data give a tunnel size of 6.9 angstroms and an increase of cyclohexane or carbon tetrachloride uptake with dehydration temperature up to 500°C. At 600°C, the tunnel structure collapses. Both Lewis and Brönsted acid sites have been observed in OMS-1. Particular applications of these materials include adsorption, electrochemical sensors, and oxidation catalysis.

There are several naturally occurring manganese oxides with one-dimensional tunnel structures, such as hollandite, which consists of MnO_6 octahedra shared by vertices and edges making (2 × 2) octahedral unit tunnels (*1–3*), romanechite with (2 × 3) tunnels (*3*, *4*), todorokite with (3 × 3) tunnels, and materials with larger tunnels like (3 × 4) and (3 × 5) (*5–14*). Todorokite appears to be the most interesting of these because it has the largest tunnel (6.9 Å) as well as cation-exchange behavior like zeolites (*5*, *11*).

Natural todorokite is poorly crystalline, impure in composition, and coexists with other manganese oxide minerals. Applications of natural todorokite have therefore been limited, and the exact identification of this material is complicated. Many fundamental questions remain concerning the chemistry of todorokite.

Manganese oxides with hollandite tunnel structures (2 × 2) have been synthesized (*15*, *16*). A large crystal of $Rb_{0.27}MnO_2$ with a 2 × 5 structure has been prepared by reaction of β-MnO_2 with RbOH in a gold capsule at 350°C and 200 MPa (*17*). Todorokite was reported to be synthesized in 1971 (*18*), but its validity was doubted (*19*). Recently, Golden *et al.* reported the hydrothermal transformation of buserite (which has a layered structure) into todorokite (*20*, *21*). Initially the layered mineral birnessite forms and is ion-exchanged to form Mg birnessite (that is, buserite). However, no thermal stability was reported for their synthetic todorokite. We used the method of Golden *et al.* (*20*, *21*) to prepare todorokite, but the structure for the resultant material was found by x-ray diffraction (XRD) and surface area measurements [Brunauer-Emmett-Teller (BET) isotherms] to collapse on calcination at 300°C after 1 hour in contrast to natural todorokites, which are stable to at least 500°C (*22*).

Hydrothermal syntheses of the polymorphs of MnO_2 from reactions of MnO_4^- and Mn^{2+} are known to depend critically on the nature of precursors (*23*) and experimental conditions (*15*, *24*). We have developed $Mg(MnO_4)_2$-$MnCl_2$ reactions for preparing stable synthetic todorokite.

Washed Mg^{2+} layered manganese oxides, which were obtained by ion exchanging Na^+-type layered manganese oxides (*25*), were autoclaved at 155° to 170°C for 10 to

Y. F. Shen, R. P. Zerger, R. N. DeGuzman, Department of Chemistry, U-60, University of Connecticut, Storrs, CT 06269.
S. L. Suib, Departments of Chemistry and Chemical Engineering and Institute of Materials Science, U-60, University of Connecticut, Storrs, CT 06269.
L. McCurdy and D. I. Potter, Department of Metallurgy and Institute of Materials Science, University of Connecticut, Storrs, CT 06269.
C. L. O'Young, Texaco Research Center, Texaco, Inc., P.O. Box 509, Beacon, NY 12508.
*To whom correspondence should be addressed.

40 hours. The autoclaved products were also filtered and washed three times with double-distilled deionized water and dried at room temperature by filtration or by freeze-drying. Samples were calcined at 200°, 300°, 400°, and 500°C in air for 1 hour.

The MnO_4^-/Mn^{2+} ratio used in the preparation of layered manganese oxide materials is a primary factor in controlling the quality of todorokite product (see below). A summary of MnO_4^-/Mn^{2+} ratios, sample nomenclature, color, and nonoxide composition of autoclaved samples is presented in Table 1. Nomenclature for calcined samples is as follows: T3C3 represents synthetic todorokite (T) with a MnO_4^-/Mn^{2+} ratio of 0.30 (3) and calcination (C) at 300°C (second 3 in acronym).

The quality of synthetic todorokite depends on the crystallinity of its layered precursors as revealed by XRD analysis (*26*). Several factors influence the crystallinity, such as the MnO_4^-/Mn^{2+} ratio, pH, temperature, aging, and autoclave procedures. Theoretically, MnO_4^-/Mn^{2+} ratio of 0.67 is necessary to prepare MnO_2 according to the following reaction:

$$2\ MnO_4^- + 3\ Mn^{2+} + 4\ OH^- \rightarrow 5\ MnO_2 + 2\ H_2O \quad (1)$$

Because the average Mn oxidation state of birnessite is 3.7, the MnO_4^-/Mn^{2+} ratio must be less than 0.67; synthetic and analytical data suggest a maximum of 0.60.

The birnessite samples B1 and B2 (as well as T1 and T2) contain Mn_2O_3 and Mn_3O_4 phases from the incomplete oxidation of Mn^{2+}. Deep oxidation leads to poorly crystalline materials (B5 and B6 or T5 and T6) with brown or black-brown colors like samples B1 and B2.

Highly crystalline birnessite, buserite, and todorokite materials are obtained for ratios of 0.3 to 0.4. For Na birnessite (MnO_4^-/Mn^{2+} ratio up to 0.40), the products are gray-black (Table 1) and show three major peaks at 7.11, 4.60, and 3.56 Å (Na-B3 and Na-B4), which are much stronger than all other (B) samples. Pure Mg^{2+} layered materials are obtained for ratios between 0.3 and 0.40 (Mg-B3 and Mg-B4), which show five major peaks at 9.74, 4.88, 4.63, 3.25, and 1.95 Å.

Unlike the XRD patterns of the layered materials, the strongest peak for the todorokites appears at 4.71 Å, instead of 9.51 Å, which probably indicates that the corresponding material is not a layer-structure material but a tunnel structure like natural todorokite (*27*). Four major peaks at 9.51, 4.71, 3.18, and 2.38 Å are observed for T3 and T4. Some natural todorokites also show four major XRD peaks at 9.6, 4.77, 3.19, and 2.40 Å, which were indexed to the (001), (002), (003), and (004) reflections, respectively, by assuming a pseudoorthorhombic cell (6). On further increasing the MnO_4^-/Mn^{2+} ratio, products become impure and crystallinity is significantly decreased (T5 and T6). A lattice parameter of 9.516 Å is calculated for T4 based on a pseudoorthorhombic cell.

The content and the Mn/Mg ratio control the degree of ion exchange of layered precursors, which are important for preparation of crystalline, pure, and thermally stable materials. The exchange capacity depends on aging temperature, the nature of cations, and drying treatment, in agreement with studies of natural layered materials (*24*). This degree of ion exchange must be related to the amount and location of lower valent manganese (Mn^{2+}). Therefore, Mg^{2+}, Ca^{2+}, or Na^+ cations in tunnels may be important for the preparation of stable todorokite materials (T4 or OMS-1). Note that Ca^{2+} is an impurity from the $KMnO_4$ (see Table 1); as MnO_4^-/N increases, so does $[Ca^{2+}]$. Ion exchange data (*28*) indeed suggest that a significant fraction of the Mg^{2+} ions can be replaced during ion exchange, supporting the idea that Mg^{2+} ions are present in tunnels. The overall $[Mg^{2+}]$ is significantly greater for OMS-1 than natural todorokite (*28*). The XRD and scanning electron microscopy–energy dispersive x-ray analysis (SEM/EDX) (*29*) results suggest that B3 and B4 are pure birnessites and appear to be different in nature from B5 and B6. Samples B3 and B4 have a layer structure, but they are not uniquely identified with respect to published data or from studies of natural manganese oxide materials. Hence, birnessite may not be the best precursor for transformation to todorokite. Because birnessite can be ion exchanged to form buserite in aqueous solution, our experimental procedures suggest that buserite, rather than birnessite, is transformed into todorokite as previously suggested (*20, 21*).

Certain preparation parameters are also important, such as pH and autoclave conditions. For example, low pH is found to be necessary to obtain hollandite or nsutite or both (*15*), whereas amorphous materials are obtained at a pH ranging from 5 to 11 (Fig. 1). Nevertheless, layered materials are prepared under strongly basic conditions. Aging is clearly important for crystal growth

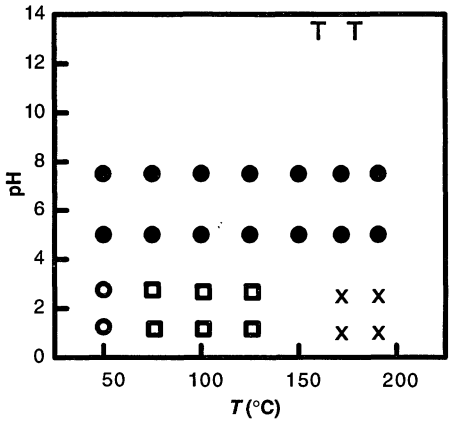

Fig. 1. Phase diagram for the synthesis of manganese oxide tunnel structures: ●, amorphous; ○, pyrolusite, 1 × 1; □, hollandite, 2 × 2; ×, nsutite, intergrowth; and T, todorokite.

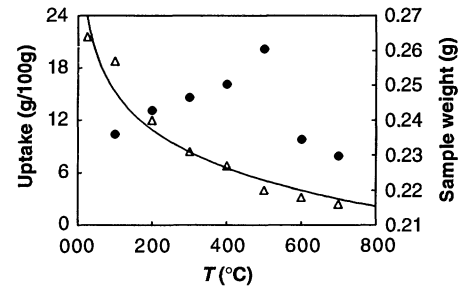

Fig. 2. Carbon tetrachloride uptake (●) and dehydration weight loss (△) as a function of temperature.

Table 1. Properties of todorokites.

Property	Todorokites					
	T1	T2	T3	T4	T5	T6
Color*	Br	Gr-Bl	Gr-Bl	Gr-Bl	Br-Bl	Br
MnO_4^-/Mn^{2+} ratio	0.20	0.25	0.30	0.40	0.50	0.60
Composition†						
Mg (%)	4.54	5.58	6.22	8.66	7.30	5.19
K (%)	0	0	0	0	1.26	1.43
Ca (%)	0.17	0.39	0.74	0.36	1.32	1.51
Mn (%)	96.01	93.76	92.20	90.00	89.70	91.76
Mg/Mn	0.048	0.060	0.067	0.096	0.081	0.057
Valency‡						
MnO_2		60.08	61.45	69.53		
MnO			21.15	17.62	5.34	
MgO			6.07	8.36	6.49	
Mn (average)			3.40	3.48	3.72	

*Colors: Br, brown; Gr, gray; and Bl, black. †Autoclaved for 8 hours at 100°C. ‡From AAS (*40*) and titration (*41*) data.

and probably controls cation distributions. High-temperature aging may help fix cations tightly in the framework of B4 so that ion exchange capacity is significantly reduced. The nonexchangeability of natural birnessite is probably due to such long aging time. Autoclave treatment of Mg^{2+}-B4 at 160° to 180°C for 5 days or longer gives only todorokite; no other crystalline phases are found.

As a consequence, the following optimal conditions are found for synthesis of todorokite: a MnO_4^-/Mn^{2+} ratio of 0.3 to 0.4, a pH of 13.8, aging at room temperature for 1 week, and autoclave treatment at 160° to 180°C for 4 to 6 days.

Because the XRD data of the OMS-1 (T4) are similar to those for natural todorokite (6), OMS-1 can be assumed to have a similar pseudoorthorhombic unit cell. Based on this assumption, the lattice parameters of OMS-1 are as follows: a = 9.516 Å, b = 10.31 Å, and c = 2.97 Å. These values are in excellent agreement with those of a Cuban todorokite studied by Faulring (*30*) which has a = 9.56 Å, b = 10.29 Å, and c = 2.84 Å. Adsorption data also support the tunnel structure of OMS-1. Carbon tetrachloride uptake increases as dehydration temperature increases (Fig. 2), indicating that tunnel water is removed with concomitant increase of uptake of various hydrocarbons until the tunnel structure collapses at 600°C. The uptake of different hydrocarbon adsorbates (Table 2) reveals the size of the tunnel to be ~6.9 Å, agreeing well with tunnel sizes of natural todorokites (*3–5, 8, 13*). In contrast to OMS-1, the Mg-layered precursor (Mg-B4) shows different uptake with dehydration temperature, further supporting the tunnel structure of OMS-1 (Fig. 3).

Fig. 3. Structure of OMS-1.

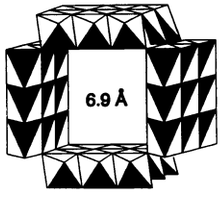

The transmission electron microscopy (TEM) (*31*) data show that the morphology of OMS-1 changes (Fig. 4A) when transformed from buserite. The hexagonal microdomains of OMS-1 shown in Fig. 4B have not been reported for natural todorokites (*3–5, 8, 13*) and may indicate some structural differences between such materials. Such structures may result from defects. The XRD data for OMS-1 in fact show slightly sharper patterns than natural materials. The TEM electron diffraction patterns (Fig. 4C) are also slightly different than for natural materials but do not show evidence of twinning or superstructures. The 3 × 3 tunnel structure has also been confirmed on the basis of TEM photos such as in Fig. 4D. Electron diffraction and TEM data for OMS-1 suggest that less twinning is observed than for natural materials (*3–5, 8, 13*).

The thermogravimetric analysis (TGA) (*32*) data for OMS-1 look similar to those for a Portuguese todorokite (*5*), which also has an abrupt weight loss at ~550°C in a N_2 atmosphere. A similar weight loss at ~550°C is shown in Fig. 5A. This weight loss is probably due to transformation of MnO_2 to Mn_2O_3 through loss of oxygen (*5*). The differential scanning calorimetry (DSC) profiles of Fig. 5B also show that OMS-1 has no significant phase transition below 550°C. The surface areas (three-point BET method, N_2 gas, Quantasorb apparatus) measured for OMS-1 materials range from 140 to 180 m^2/g and are consistent with surface areas measured for manganese nodules used by Weisz (*33*) for catalytic oxidations of CO, CH_4, and butane.

The XRD results also support the conclusion that thermally stable synthetic todorokite materials (OMS-1) have been prepared in contrast to other reported materials (*20, 21, 27*). OMS-1 still has a weak peak at 9.3 Å when calcined at 500°C for 1 hour, as is the case for natural todorokite. These results indicate that OMS-1 is stable up to 500°C.

The differences between OMS-1 and previously reported materials of Golden *et al.* (*20, 21*) are presently not well understood; however, it is clear that structural, chemical, and physical properties of these two classes of materials are markedly different. For example, the lattice parameters, thermal stabilities, and chemical compositions are not the same for OMS-1 and materials reported earlier (*20, 21*). Different phases of both synthetic and natural todorokites may exist. Another distinction of OMS-1 materials is that ions similar to Mg^{2+} in size, charge, and polarizability, such as Zn^{2+}, Ni^{2+}, Co^{2+}, and Cu^{2+}, can be substituted for Mg^{2+} ions and result in thermally stable, crystalline OMS-1 derivatives, which was not found to be the case in earlier research (*20, 21*).

As for oxidation states, electron paramagnetic resonance (EPR) (*34*) results suggest the presence of Mn^{2+} ions in octahedral sites based on a separation of 99 G.

Table 2. Uptake of adsorbates in OMS-1 heated to 500°C.

Adsorbate	c-C_6H_{12}	CCl_4	1,3,5-Triethylbenzene	Hexachlorobutadiene
Dimension (Å)	6.1	6.9	8.4*	7.7*
Uptake (g/100 g)	18.2	20.0	0	0

*Estimated from bond length and atomic radius.

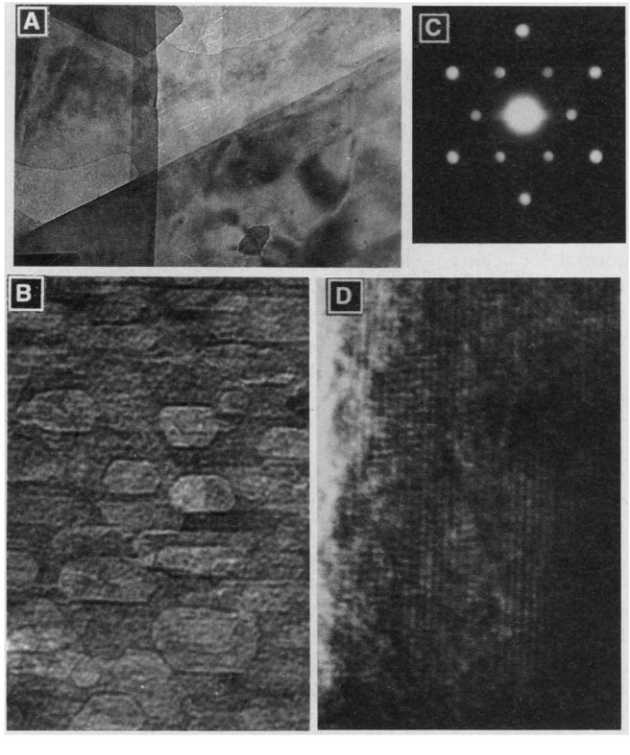

Fig. 4. Transmission electron micrographs (TEMs) of (**A**) sample B-4 and (**B**) sample T4. In (A), the plates are featureless and have dimensions of about 2400 Å. Sample T4 consists of plates of similar dimensions to B-4, as well as interlocking hexagonal features. The dimensions of these hexagonal features are about 100 Å by 250 Å. (**C**) An electron diffraction pattern for single crystalline T4, which shows pseudoorthorhombic symmetry. Lattice parameters for b and c of 10.31 Å and 2.97 Å, respectively, were determined from such electron diffraction data, again based on a pseudoorthorhombic cell. (**D**) A TEM image showing the 3 × 3 tunnel structure of T4. No such tunnel structures were observed for the B4 precursor layered material.

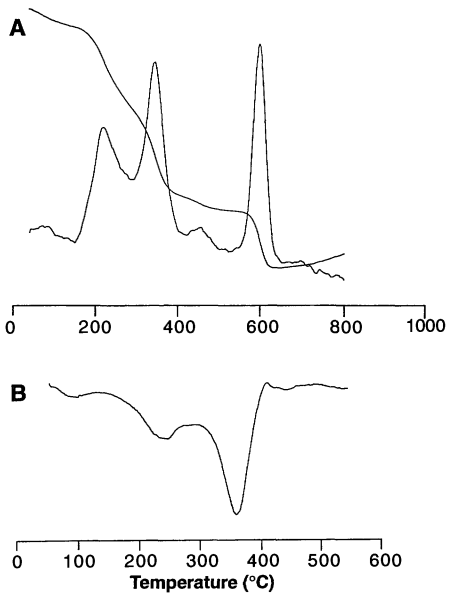

Fig. 5. Analysis of T4 by (**A**) TGA and (**B**) DSC. Todorokite (*4*) undergoes a loss in weight up to 250°C due to the loss of water in the tunnel (*5*). There is an abrupt weight loss at ~670°C in an O_2 atmosphere. In addition, there is divergence of the O_2 and N_2 TGA results, suggesting that oxygen evolution begins around 250°C. Water content is estimated from the O_2 curve to be ~12.5% by weight. The significant endothermic transition in the DSC data centered at 359°C is due to loss of water and to some loss of oxygen from the lattice based on temperature programmed desorption, reduction, oxidation, and oxygen mobility studies (*22*).

Table 3. Reduction and oxidation potentials for manganese oxides. Numbers in parentheses represent current in milliamperes; x, not observed; c, cathodic wave; and a, anodic wave.

Sample	Potential (V)		
	pH 5.0	pH 7.0	pH 10.0
Pyrolusite	x	x	c 0.15 (100) −0.42 (125) a 0.30 (125)
Manganite	c 0.65 (1.17) −0.15 (1.00) −0.72 (4.83) a 0.83 (267)	x	x
Hollandite	c 0.42 (16.7) −0.15 (75) a 0.83 (158)	c x a 0.50 (217)	c 0.08 (200) −0.40 (192) a 0.30 (317)
Birnessite	c −0.72 (45.8) a 0.85 (43.8)	c x a 0.78 (150)	c 0.12 (175) −0.30 (192) a 0.30 (167) 0.78 (300)
Todorokite	c 0.60 (5.00) −0.15 (9.17) −0.65 (6.67) a 0.90 (18.3)	c 0.50 (6.67) −0.95 (28.3) a 0.78 (30.0)	c 0.18 (41.7) −0.85 (50.0) a 0.20 (41.7) 0.65 (66.7)
Synthetic birnessite	c 0.90 (50) 0.50 (8) a −0.74 (40)	c −0.76 (42) a −0.75 (48)	c 0.68 (117) 0.25 (75) a −0.05 (83)
OMS-1	c 0.45 (13.3) a 0.85 (50.0)	c 0.42 (12.5) a 0.75 (70.8)	c 0.10 (43.3) −0.23 (38.3) a 0.70 (95.0)

Two less intense peaks in between the major peaks are observed which are likely due to forbidden transitions. Similar observations have been reported in zeolitic materials and the additional lines are assigned to forbidden transitions of $\Delta mI = +1$ (*35*, *36*). In addition, the asymmetry of the hyperfine peaks may be an indication of quadrupole interactions in synthetic todorokite. These EPR results conclusively show the existence of Mn^{2+} in synthetic solid manganese oxide materials and leads to the conclusion that the lower valent manganese is indeed Mn^{2+}, which agrees with suggestions of others (*6*, *17*) that Mn^{2+} is present in natural todorokite (*6*, *27*).

On the basis of 12 oxygen atoms per unit cell (not including H_2) and the above data, one can write a general formula for OMS-1 as $(Mg^{2+}\ 0.98–1.35\ Mn^{2+}\ 1.89–1.94\ Mn^{4+}\ 4.38–4.54)O_{12}{\cdot}4.47–4.55\ H_2$. This formula is similar to natural todorokites, which have a wide range of chemical composition and a general formula (Na, Ca, K, Ba, Sr)0.3–0.7(Mn, Mg, Al)$_6O_{12}$ 3.2–4.5 H_2O (*5*, *12*).

Cyclic voltammetry data (Table 3) (*37*) suggest that redox potentials and currents can be used to distinguish various manganese oxide minerals and synthetic samples. As many as three cathodic waves are observed for the samples, being associated with redox reactions of Mn^{4+}, Mn^{3+}, and Mn^{2+}.

The overall potential range of the different materials is quite similar. As pH increases, the observed currents increase substantially. The cyclic voltammetry data show quasi-reversible electrochemical behavior, indicating that chemical reactions at these pH values are minimized. Apparently, these materials are stable in the pH range used for these studies, in agreement with XRD data from our labs.

A strong band for pyridine adsorbed on Lewis (L) acid sites in OMS-1 was observed in Fourier transform infrared spectroscopy (FTIR) (*38*) when desorption is performed at 100°C. A very broad band, consisting of several IR peaks, is detected in the range from 1530 to 1630 cm^{-1}. At 200°C, both the L-band and the broad band largely decrease in intensity. At 300°C, both bands disappear. Thus manganese oxide tunnel structures such as OMS-1 have acid sites, including both Lewis and Brönsted sites. Possible applications include acid-catalyzed reactions such as isomerizations and polymerizations. Manganese oxide materials are well-known oxidation catalysts (*33*).

For OMS-1, the conversion of methane was found to be 32.5% with selectivities for C_2H_4 of 13%, for C_2H_6 and C_2H_2 of 35%, for C_3H_6 of 3%, for C_3H_8 of 5%, for all total C_4 species of 23%, and for C_{5+} species of 21% (*39*). No significant coke formation was observed in the reactor or on the catalyst during these experiments.

A final area of potential application includes electrochemical devices. It can be shown with cyclic voltammetry (*28*) that molecules can be distinguished on the basis of both size and charge by incorporating OMS-1 into electrodes. Molecules larger than 6.9 Å or anions in solution are not electroactive, consistent with the pore size of OMS-1 and its ability to exchange cations rather than anions. In addition, the conductivity of OMS-1 markedly increases above 275°C and reversibly decreases in conductivity as temperature is again lowered, even after several cycles. No apparent structural phase transitions have been observed in this temperature range for OMS-1 based on XRD or DSC-TGA data, which may indicate an electronic phase change or, for example, a change in the density of states at temperatures above 275°C.

REFERENCES AND NOTES

1. A. Clearfield, *Chem. Rev.* **88**, 125 (1988).
2. J. E. Post and C. W. Burnham, *Am. Mineral.* **71**, 1178 (1986).
3. S. Turner and P. R. Buseck, *Science* **203**, 456 (1979).
4. S. Turner and J. E. Post, *Am. Mineral.* **73**, 1155 (1988).
5. D. L. Bish and J. E. Post, *ibid.* **74**, 177 (1989).
6. J. A. Straczek, A. Horen, M. Ross, C. M. Warshaw, *ibid.* **45**, 1174 (1960).
7. F. V. Chukhrov *et al.*, *Nature* **278**, 631 (1979).
8. S. Turner and P. R. Buseck, *Science* **212**, 1024 (1981).
9. V. M. Burns and R. G. Burns, *Am. Mineral.* **63**, 827 (1978).
10. F. V. Chukhrov, A. I. Gorshkov, A. V. Sivtsov, V. V.

Beresovskaya, *Izv. Akad. Nauk SSSR Geol.* **12**, 86 (1978).
11. D. L. Bish and J. E. Post, *Geol. Soc. Am. Abstr. Prog.* **16**, 625 (1984).
12. J. Ostwald, *Mineral. Mag.* **50**, 336 (1986).
13. J. E. Post and D. L. Bish, *Am. Mineral.* **73**, 861 (1988).
14. R. G. Burns, V. M. Burns, H. W. Stockman, *ibid.* **68**, 972 (1983).
15. C. L. O'Young, in *Synthesis of Microporous Materials*, M. Occelli and H. Robson, Eds. (Van Nostrand Reinhold, New York, 1992), vol II, p. 333.
16. N. Yamamoto, T. Endo, M. Shimada, T. Takada, *Jpn. J. Appl. Phys.* **13**, 723 (1974).
17. O. Tamada and N. Yamamoto, *Mineral. J.* **13**, 180 (1986); N. Yamamoto and O. Tamada, *J. Cryst. Growth* **73**, 199 (1985).
18. R. M. McKenzie, *Mineral. Mag.* **38**, 294 (1971).
19. R. M. Porter and G. R. Rossman, *Am. Mineral.* **64**, 1199 (1979).
20. D. C. Golden, C. C. Chen, J. B. Dixon, *Clays Clay Miner.* **35**, 271 (1987).
21. _____, *Science* **231**, 717 (1986).
22. Y.-F. Shen, R. Zerger, S. L. Suib, L. McCurdy, D. I. Potter, C. L. O'Young, unpublished results.
23. S. Bach, M. Henry, N. Baffier, J. Livage, *J. Solid State Chem.* **88**, 325 (1990).
24. J. Pattanayak, V. Sitakara Rao, H. S. Maiti, *Thermochim. Acta* **151**, 193 (1989).
25. To synthesize Na^+-type oxides, $Mn(OH)_2$ sol was obtained by adding 50 ml of 5.0 M NaOH into 40 ml of 0.50 M $MnCl_2$ solution under vigorous stirring. The $Mn(OH)_2$ was then added dropwise to different amounts of 0.10 M $Mg(MnO_4)_2$ solution under vigorous stirring to prepare layered manganese oxides. The final pH for all sample suspensions was 13.8. The suspensions were aged at room temperature for 8 days and then filtered and washed with distilled deionized water (DDW) until no Cl^- was detected. Mg^{2+}-type layered manganese oxides were obtained by ion-exchanging the Na^+-type layered manganese oxides with 1 liter of M $MgCl_2$ while stirring at room temperature overnight. The exchanged products were filtered and washed three times with DDW.
26. An aqueous sample suspension was put on a glass slide and dried in air at room temperature. XRD powder patterns were obtained with a Scintag XDS-2000 θ-θ diffractometer with Cu Kα radiation (45 kV and 40 mA). Two incident slits of 2 and 4 mm were used. Samples were ground to the same particle size. Voltages and currents were held constant for all experiments which were done in a 1-week period to avoid fluctuations in x-ray beam parameters. Complete XRD data summaries are available from the authors.
27. D. C. Golden, J. B. Dixon, C. C. Chen, *Clays Clay Miner.* **34**, 511 (1986).
28. R. DeGuzman, Y. F. Shen, S. L. Suib, B. R. Shaw, C. L. O'Young, in preparation.
29. The SEM/EDX spectra were taken in an AMRAY Model 1800D SEM equipped with PV9800 EDX spectrometer. An acceleration potential of 25 kV was used for the EDX measurements. Multispot analyses were done on different particles of a sample in order to obtain more accurate information regarding lateral and bulk homogeneity. Quantitative calculations were done with the Super Quant program with a ZAF correction to obtain relative concentrations.
30. G. M. Faulring, in *Advances in X-ray Analysis*, M. Mueller, Ed. (Plenum, New York, 1962), pp. 117–126.
31. Powdered samples were ground before they were dispersed into either acetone or ethanol and ultrasonically vibrated. Fine particles were then put onto a carbon-coated Cu grid for the TEM measurements. The TEM images and electron diffraction patterns were obtained with a Phillips EM-420 analytical electron microscope (AEM).
32. Thermal analyses of the air-dried samples were carried out with a DuPont 910 DSC. The TGA experiments were done in a DuPont 951 instrument. About 3- to 10-mg samples were used.
33. P. B. Weisz, *J. Catal.* **10**, 407 (1968).
34. The EPR spectra of a sample diluted with silica gel (S-157, Fisher Scientific) were obtained with a Varian E-3 EPR spectrometer at 9.05 GHz, 77 K, and 0.5 mW of power.
35. J. Rubio, E. Munoz, P. J. Boldu, O. Y. Chen, M. M. Abraham, *J. Chem. Phys.* **70**, 633 (1979).
36. H. W. de Wijn and R. F. van Balderen, *ibid.* **46**, 1381 (1967).
37. Cyclic voltammetry experiments were done on a BAS Model 100 electrochemical apparatus. (A saturated calomel electrode was used as a reference and a Pt wire was used as a counterelectrode.) Working electrodes of manganese oxide minerals and synthetic manganese oxides were prepared by taking 20 to 40% by weight manganese oxide and mixing it with carbon paste. Working electrodes were made by connecting the carbon paste manganese oxide mixtures to a copper wire. Electrolyte solutions were prepared from K and Na phosphate buffers of pH 5.0, 7.0, and 10.0 from pHydrion Buffers. Argon gas bubbled through the electrolyte solution for at least 10 min to remove oxygen gas. Several cycles were typically done in order to follow changes in reductions and oxidations on cycling.
38. A self-supported manganese oxide sample wafer was dehydrated in vacuum at 400°C for 3 hours. The sample wafer was then cooled to 100°C and exposed to pyridine vapor for 0.5 hours. Desorption was conducted at 100°, 200°, and 300°C each for 1 hour before IR spectra were recorded at room temperature with a GL-6020 Galaxy Series FT-IR spectrometer.
39. Oxidation of methane was carried out by using a 1/4 wave Evenson microwave cavity and by flowing CH_4 at a flow rate of 50 ml/min at a pressure of 20 torr in a quartz reactor that has previously been described [S. J. Suib and Z. Zhang, U.S. Patent 5 015 349 (1991); P. R. Zerger and S. L. Suib, *J. Catal.* **139**, 383 (1993)]. Synthetic todorokite was placed downstream of the plasma zone at ambient temperature. Products were analyzed on stream with gas chromatography methods. The thermal temperatures in the plasma are typically between 75° and 150°C. The electronic temperatures in the plasma are likely near 2000 K.
40. Compositions were analyzed with a Varian Techtron AA-6 atomic absorption spectrophotometer (AAS) with a nitrous oxide–acetylene flame. The standard for Mn was Mn metal dissolved in 5% nitric acid, which was diluted with 1% nitric acid. About 50 mg of synthetic todorokite sample dried at 120°C was dissolved with 20 ml of DDW, 1 ml of concentrated nitric acid, and 2 ml of 30% hydrogen peroxide. The colorless solution was boiled for 2 to 5 min to remove excess peroxide and the solution was diluted with DDW to 100 ml to make a stock solution. Manganese was analyzed by using the standard addition method.
41. J. M. Murray, L. S. Balistieri, B. Paul, *Geochim. Cosmochim. Acta* **48**, 1237 (1984).
42. We acknowledge the support of the Department of Energy, Office of Basic Energy Sciences, Division of Chemical Sciences, and Texaco, Inc. for support of this research. We thank A. Clearfield, J. Dixon, and L. R. Faulkner for helpful discussions. Helpful discussions with B. R. Shaw on electrochemical studies are appreciated. We thank C. Francis of the Harvard Mineralogical Museum for loan of various manganese oxide minerals including pyrolusite (cat. no. 100686), manganite (cat. no. 131562), hollandite (cat. no. 106790), birnessite (cat. no. 1007575), and todorokite (cat. no. 104794).

6 October 1992; accepted 21 January 1993

Vapor-Condensation Generation and STM Analysis of Fullerene Tubes

Maohui Ge and Klaus Sattler

Fullerene tubular structures can be generated by vapor condensation of carbon on an atomically flat graphite surface. Scanning tunneling microscope (STM) images revealed the presence of tubes with extremely small diameters (from 10 to 70 angstroms), most of which are terminated by hemispherical caps. Atomic resolution images of such structures showed that the tubes have a helical graphitic nature. The formation of the tubes under the quasi-free conditions suggests that the growth to tubular rather than spherical configurations is preferred for "giant fullerenes."

Despite the tremendous interest recently in the physics and chemistry of C_{60} and other fullerenes and their solid forms, little is known about fullerene growth. Neither the onset of nucleation nor the progression toward the fullerene network is understood. The structure of giant fullerenes (containing hundreds of carbon atoms) is also controversial; experimental evidence exists to support two possibilities, spherical molecules versus tubular cages.

Concentric tubular carbon structures were recently found by transmission electron microscopy at the end of carbon rods used for arc discharge (*1*, *2*), and such structures could be produced in macroscopic quantities by using a similar generation method (*3*). The smallest inner tube that was observed (*1*) had a diameter of 22 Å. Electron diffraction pattern revealed helical arrangement for concentric graphitic networks. The tubes were grown out from a carbon substrate. Therefore a direct comparison to the free fullerene growth could not be made. Although various properties of the tubules were measured, the atomic structure could not be directly determined.

Recent calculations predict that carbon tubules of different diameters and helicities have striking variations in electronic transport, from metallic to semiconducting (*4*–*7*). Also, such tubules are expected to shield guest atoms from external electric and magnetic fields (*8*). Besides tubular structures, other low-energy configurations

Department of Physics and Astronomy, University of Hawaii, Honolulu, HI 96822.